Supplement of

Distinct chemical and mineralogical composition of Icelandic dust compared to North African and Asian dust

Clarissa Baldo et al.

Correspondence to: Zongbo Shi (z.shi@bham.ac.uk)

Table S1: Sampling sites.

Dust Hotspot	Location	Sample Code	Latitude / Longitude
Dyngjusandur	NE Iceland	D3	64°50'41.885"N / 16°59'40.78"W
Hagavatn	Central W Iceland	H55	64°28'52.04"N / 20°27'18.81"W
Landeyjarsandur	S Iceland	Land1	63°34'13"N / 20°02'31"W
Mælifellssandur	Central S Iceland	Mæli2	63°48'42.2"N / 19°07'02.5"W
Myrdalssandur	S Iceland	MIR45	63°32'42.08"N / 18°42'14.14"W

Table S2: Complex refractive indexes of the individual minerals used in this study.

Mineral	Reference
Hematite	Longtin et al. (1988)
Hematite	Bedidi and Cervelle (1993)
Goethite	Bedidi and Cervelle (1993)
Magnetite	Querry (1985)
Magnetite	Huffman and Stapp (1973)
Olivine	Fabian et al. (2001)
Augite	Egan and Hilgeman (1979)
Feldspar	Egan and Hilgeman (1979)
Quartz	Khashan and Nasif (2001)
Basaltic glass	Pollack et al. (1973)

Table S3: Amorphous Fe (FeA), dithionite Fe (FeD, Hematite + Goethite), magnetite (FeM), initial Fe solubility (Fe_{isol}) and potential Fe solubility (Fe_{psol}) as extracted-dissolved Fe to total dust mass. The standard deviation (sd) is reported, n = 3. For Fe_{psol}, sd was estimated based on the relative standard deviation obtained for a dust sample from Africa (Libya), n = 7.

Samples	FeA wt% (sd)	FeD wt% (sd)	FeM wt% (sd)	Fe_{isol} wt% (sd)	Fe_{psol} wt% (sd)
D3	0.1 (0.02)	0.44 (0.04)	1.76 (0.26)	0.07 (0.002)	3.35 (0.14)
H55	0.04 (0.004)	0.33 (0.02)	1.5 (0.20)	0.01 (0.001)	1.78 (0.07)
Land1	0.14 (0.03)	0.77 (0.09)	0.87 (0.02)	0.01 (0.001)	2.12 (0.09)
Maeli2	0.18 (0.006)	0.79 (0.03)	1.66 (0.10)	0.03 (0.003)	3.39 (0.14)
MIR45	0.04 (0.001)	0.13 (0.002)	1 (0.06)	0.01 (0.001)	1.75 (0.07)

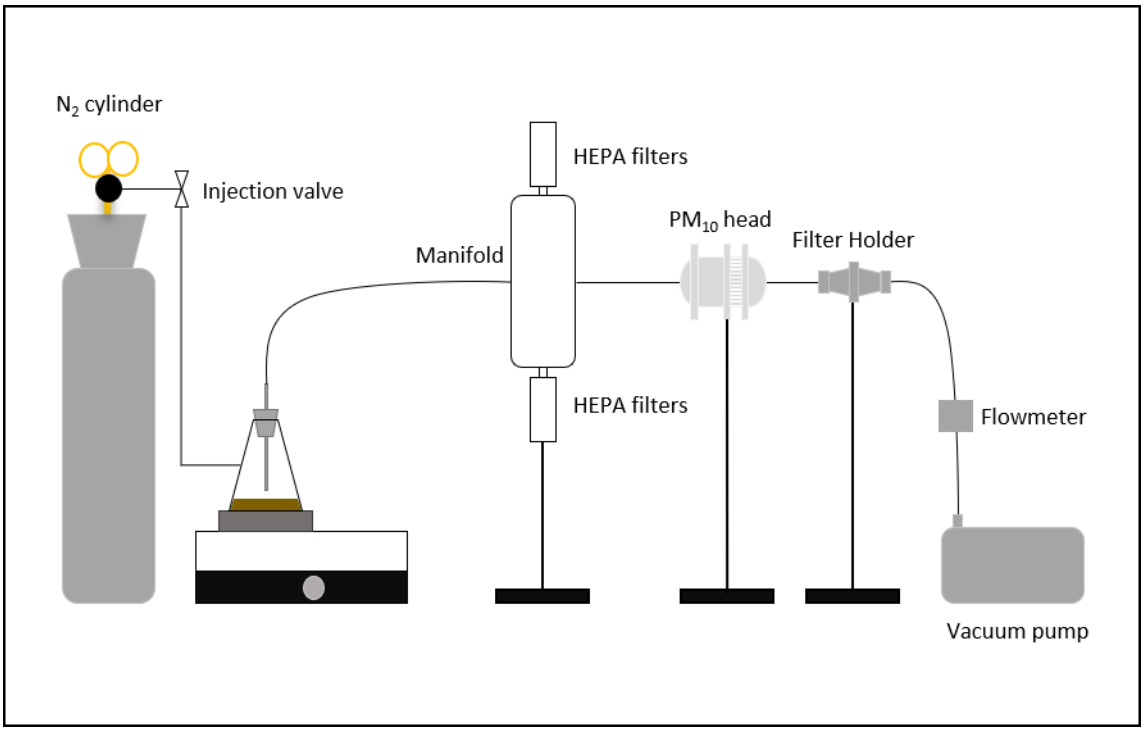

Figure S1: PM_{10} collection system.

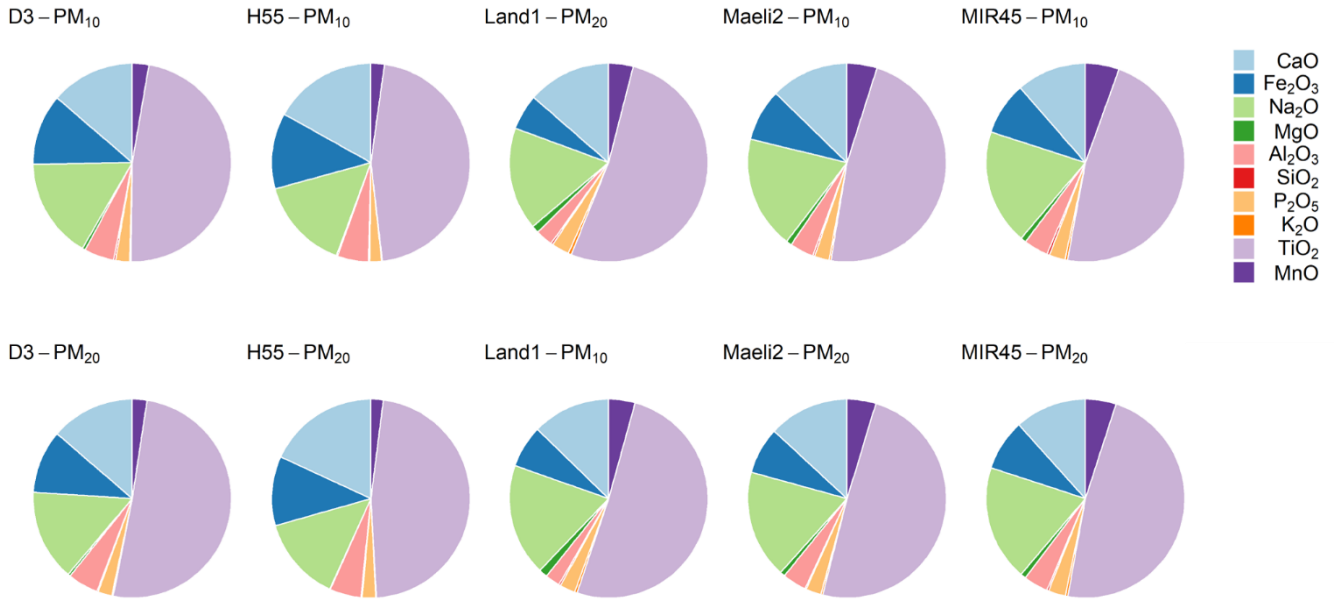

Figure S2: Element oxide mass percentages of PM_{10} (custom-made reactor) and PM_{20} (CESAM chamber). The data uncertainty is ~12%, estimated using the error propagation formula.

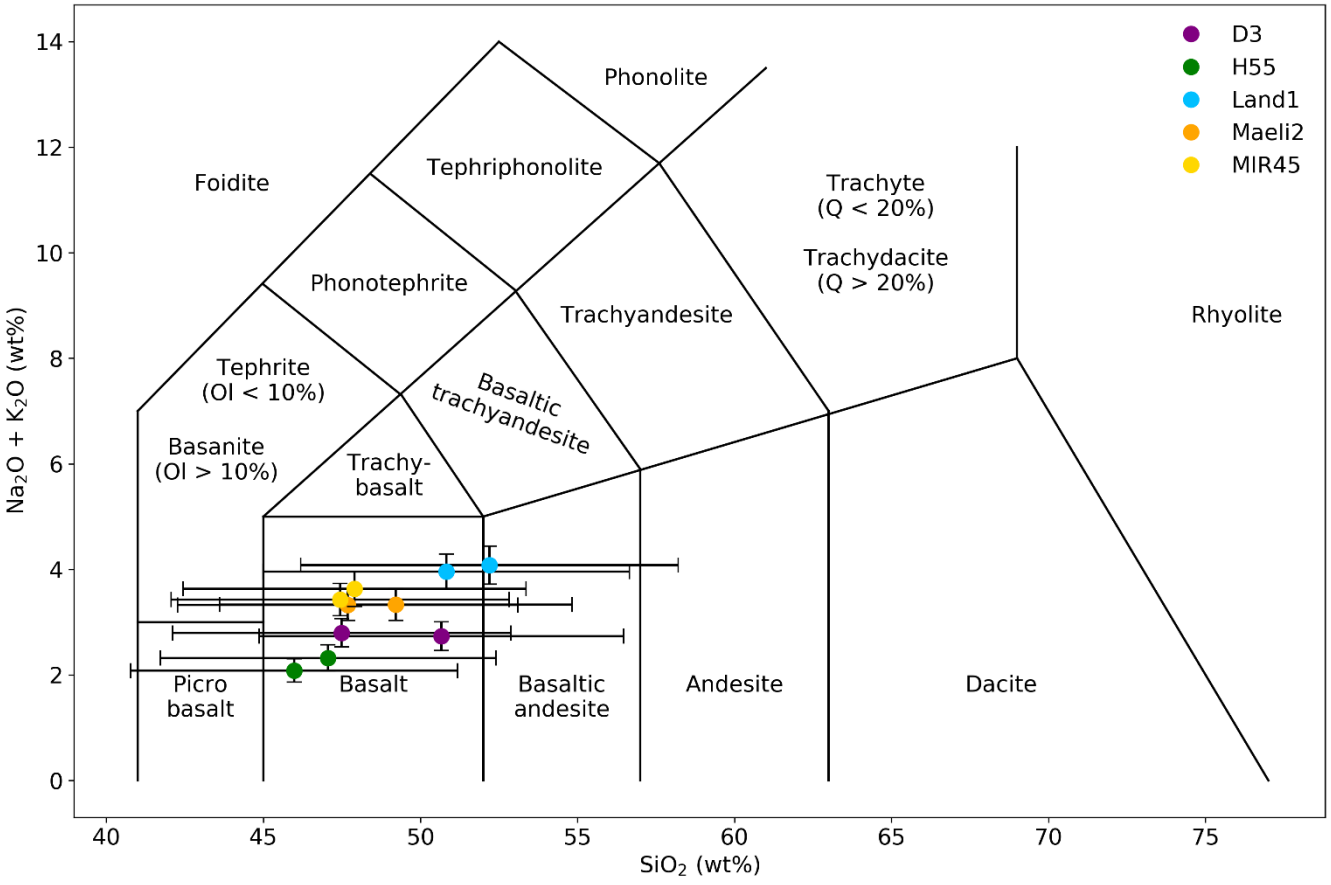

Figure S3: Classification of the dust samples (PM_{10} and PM_{20} fractions) based on the total alkali and silica (TAS) contents from the XRF measurements. The data uncertainty was estimated using the error propagation formula.

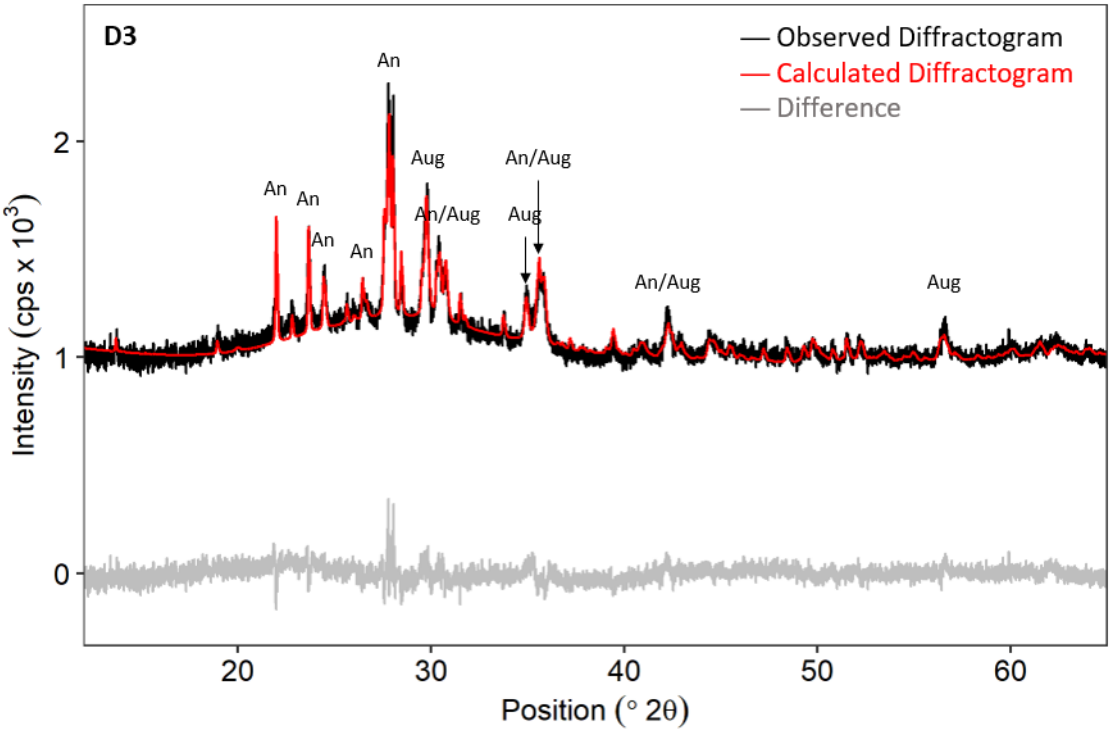

An = Anorthite #98-010-0235, Aug = Augite #98-003-4194

Figure S4: Diffractogram of D3, PM_{10} fraction. The black curve corresponds to the experimental data and the red curve to the model by MAUD software. The grey curve is the difference between the observations and the model.

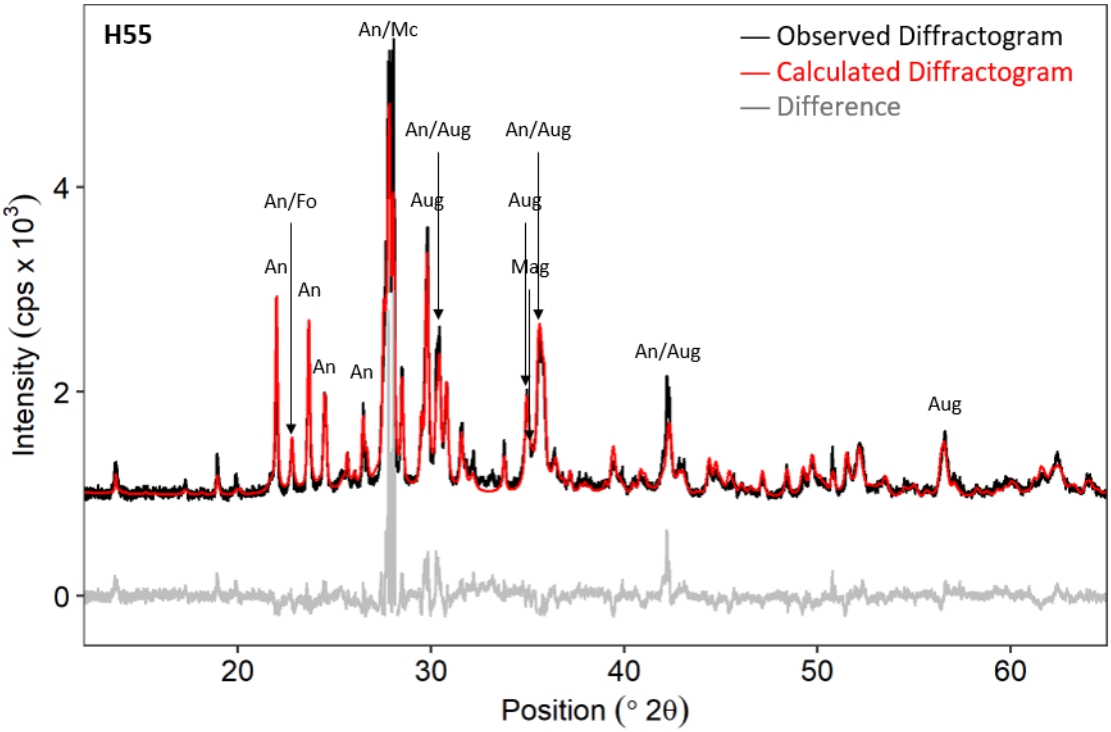

An = Anorthite #98-010-0235, Aug = Augite #98-003-4194, Fo = Forsterite #98-003-4112,
Mag = (Titano)Magnetite #98-016-2356, Mc = Microcline #98-008-3534

Figure S5: Diffractogram of H55, PM_{10} fraction. The black curve corresponds to the experimental data and the red curve to the model by MAUD software. The grey curve is the difference between the observations and the model.

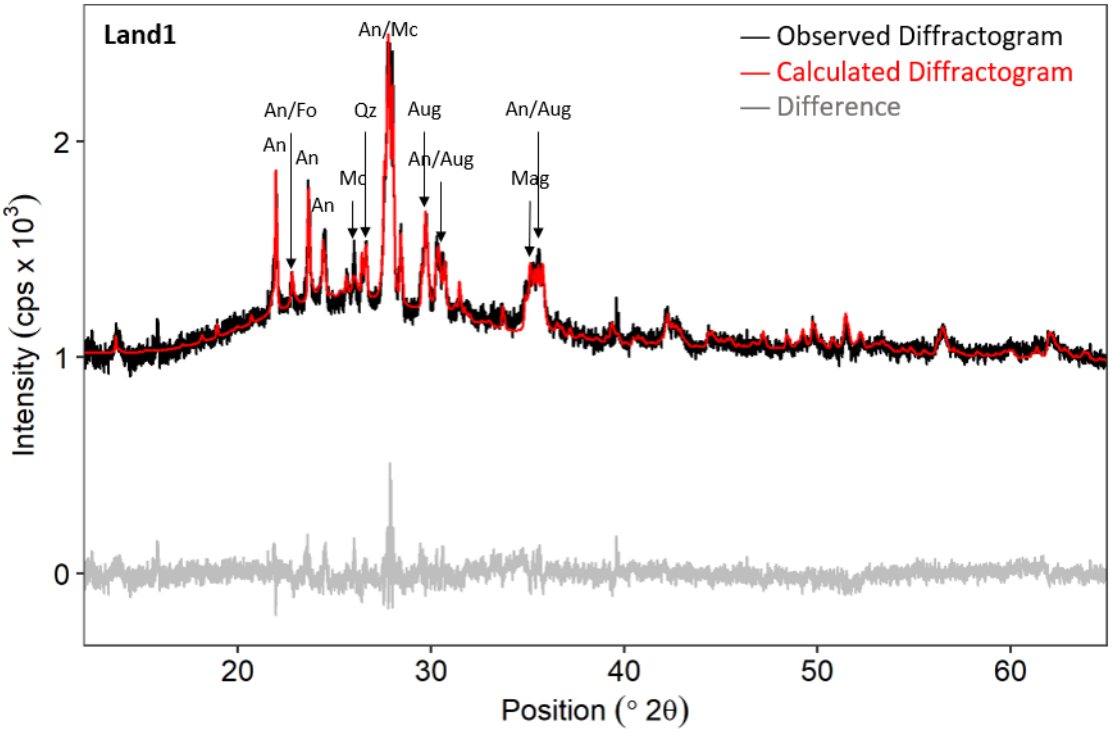

An = Anorthite #98-010-0235, Aug = Augite #98-003-4194, Fo = Forsterite #98-003-4112,
Mag = (Titano)Magnetite #98-016-2356, Mc = Microcline #98-008-3534, Qz = Quartz #98-009-3093

Figure S6: Diffractogram of Land1, PM_{10} fraction. The black curve corresponds to the experimental data and the red curve to the model by MAUD software. The grey curve is the difference between the observations and the model.

45

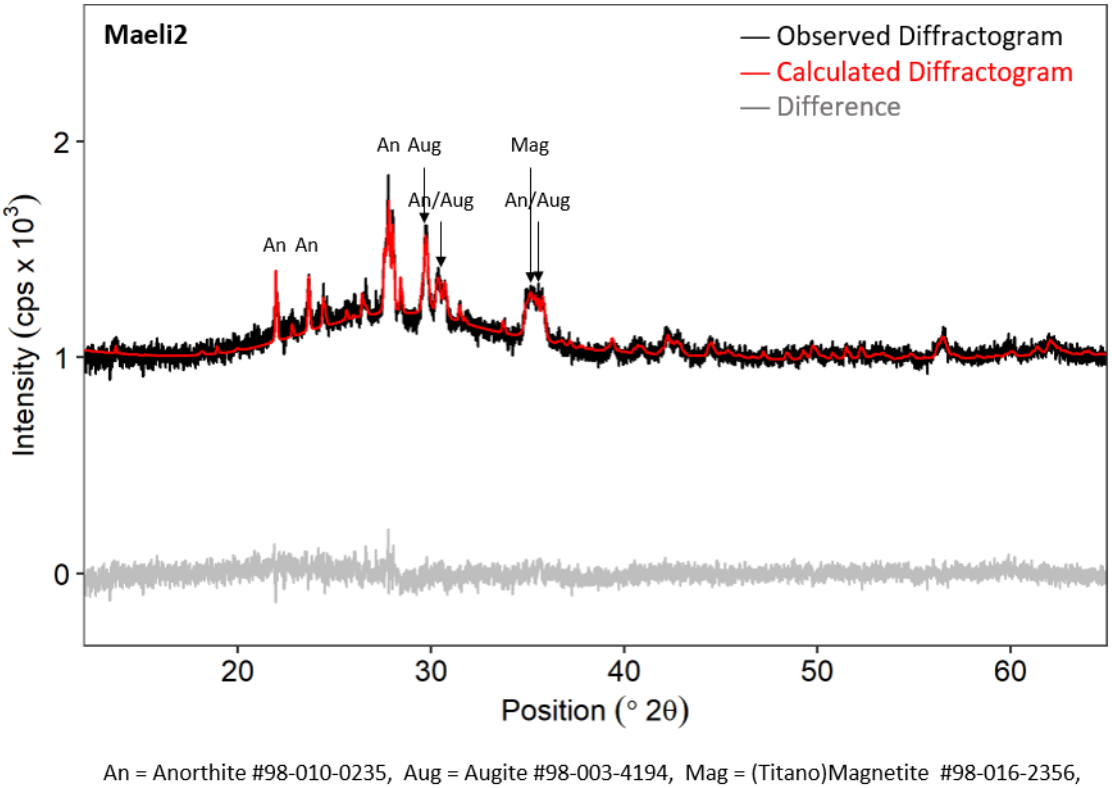

An = Anorthite #98-010-0235, Aug = Augite #98-003-4194, Mag = (Titano)Magnetite #98-016-2356,

Figure S7: Diffractogram of Maeli2, PM_{10} fraction. The black curve corresponds to the experimental data and the red curve to the model by MAUD software. The grey curve is the difference between the observations and the model.

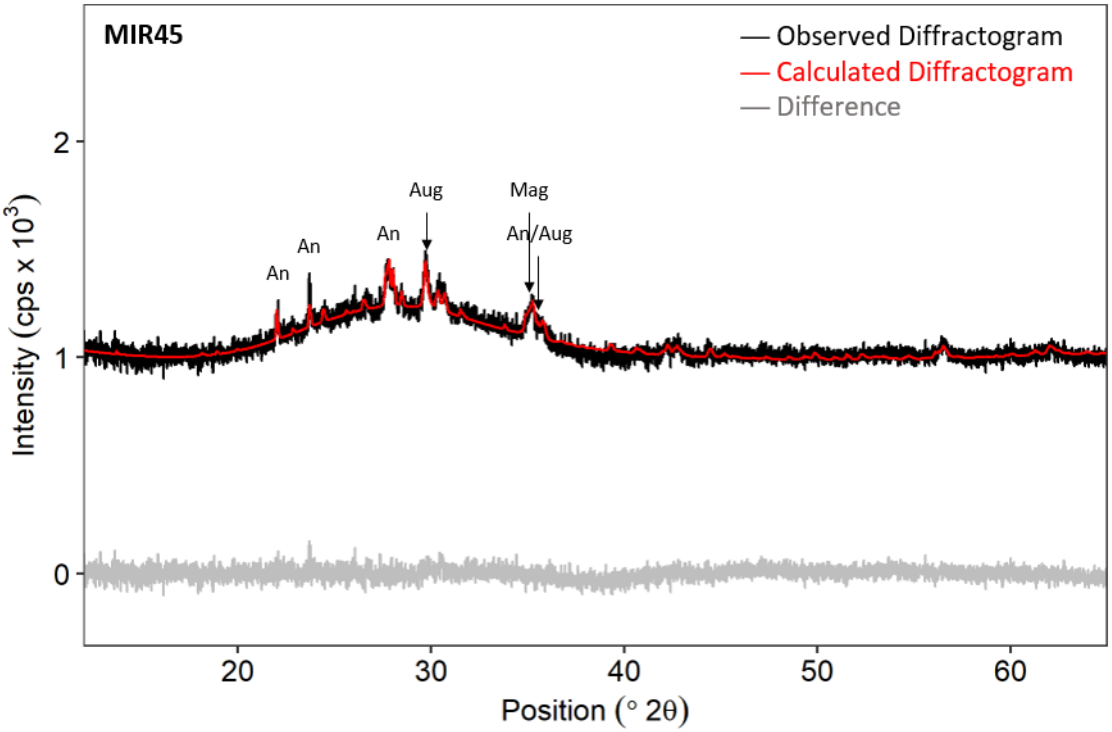

Figure S8: Diffractogram of MIR45, PM_{10} fraction. The black curve corresponds to the experimental data and the red curve to the model by MAUD software. The grey curve is the difference between the observations and the model.

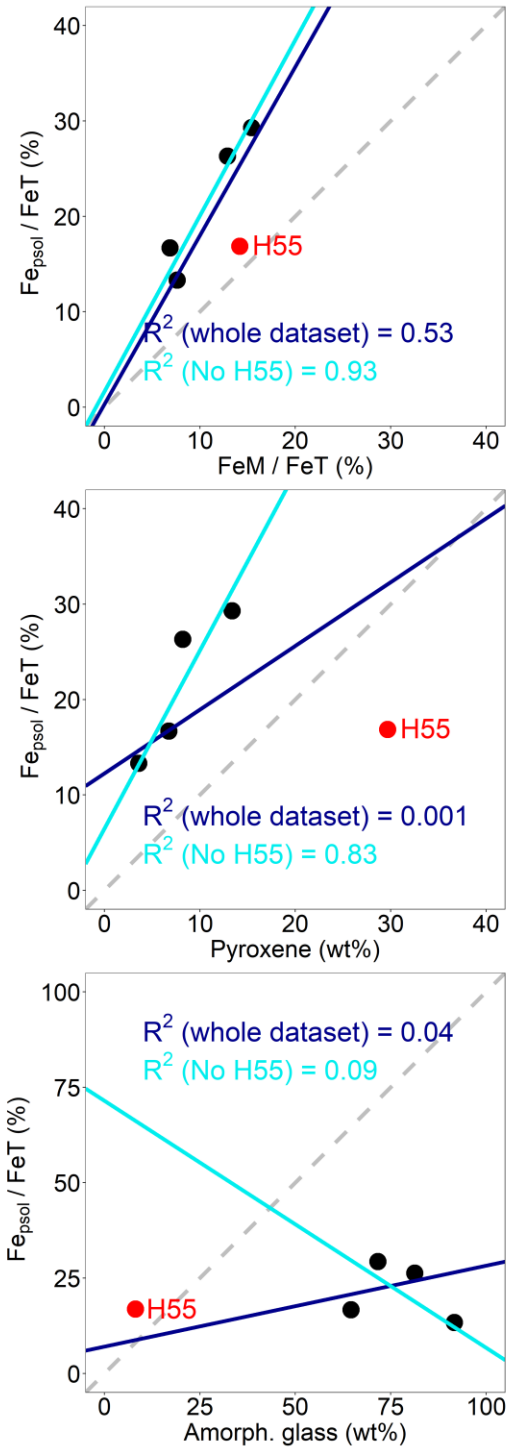

Figure S9: Correlation of Fe_{psol} / FeT (%) with the content of magnetite (FeM / FeT, %), pyroxene (wt%) and amorphous glass (wt%). The regression line in blue was calculated based on the whole dataset. The regression line in light blue was calculated excluding H55 (the dust sample with the lowest amorphous fraction).

References

Bedidi, A., and Cervelle, B.: Light scattering by spherical particles with hematite and goethitelike optical properties: effect of water impregnation, Journal of Geophysical Research: Solid Earth, 98, 11941-11952, doi: 10.1029/93JB00188, 1993.

Egan, W., and Hilgeman, T.: Optical Properties of Inhomogeneous Materials: Applications to Geology, Astronomy, Chemistry and Engineering Academic Press, New York, 1979.

Fabian, D., Henning, Th., Joger, C., Mutschke, H., Dorschner, J., Werhan, O.: Olivine, EODG ARIA, available at http://eodg.atm.ox.ac.uk/ARIA/data?Minerals/Olivine/non-oriented_(Fabian_et_al._ 2001)/olivine_Fabian_2001.ri (last access: 02 January 2020), 2001.

Huffman, D. R., and Stapp, J. L.: Optical measurements on solids of possible interstellar importance, in: Interstellar dust and related topics, Springer, 297-301, 1973.

Khashan, M. A. and Nasif, A. Y.: Quartz, EODG ARIA, available at http://eodg.atm.ox.ac.uk/ARIA/data?Minerals/Quartz/(Khashan_and Nassif_2001)/quartz_Khashan_2001.ri (last access: 02 January 2020), 2001.

Longtin, D. R., Shettle, E. P., Hummel, J. R., and Pryce, J. D.: A wind dependent desert aerosol model: Radiative properties, AFGLTR-88-0112, Air Force Geophysics Laboratory, Hanscom AFB, MA, 1988.

Pollack, J. B., Toon, O. B., and Khare, B. N.: Optical properties of some terrestrial rocks and glasses, Icarus, 19, 372-389, 1973.

Querry, M. R.: Magnetite, Refractive index database, available at https://refractiveindex.info/?shelf=main&book=Fe3O4& (last access: 02 January 2020), 1985.